

# The time-marched fast-field program (FFP) for modeling acoustic pulse propagation

Michael B. Porter

SACLANT Undersea Research Centre, I-19026 La Spezia, Italy

(Received 21 June 1989; accepted for publication 24 November 1989)

Fast-field programs (FFPs) have emerged as an important tool for predicting transmission loss in an ocean waveguide. Such models have been primarily used for time-harmonic sources; however, pulses or other broadband sources may be treated by Fourier synthesis. A new technique is developed that provides a *direct* solution by marching the solution forward in time. As an example of the method, a pulse incident on an interface between two homogeneous half-spaces is considered. Snapshots of the pulse in time illustrate graphically the effects on the reflected and transmitted waves. Second, an interesting hyperbolic cosine profile is considered that leads to repeated focusing as the pulse propagates out in range.

PACS numbers: 43.30.Bp, 43.20.Mv

## INTRODUCTION

Models for predicting the sound level due to a *time-harmonic* source in ocean acoustic waveguides have reached a high level of development. Given the time-harmonic source function, the original wave equation is reduced to a Helmholtz equation. Direct solution by finite elements or finite differences is seldom used; however, most problems can be treated adequately using parabolic equation (PE), normal mode (NM), fast-field program (FFP), or ray/beam techniques, depending on the particular approximations that can be made for the problem under consideration.

Our interest here turns to problems involving arbitrary source time series. Given the high state of development of codes for time-harmonic sources, one obvious thing to do is simply run the time-harmonic models for a number of frequencies and combine the resulting solutions with the weighting and phasing implied by the source function. In fact, a recently developed package exists which does exactly this and has been applied successfully to a wide variety of ocean acoustic problems.<sup>1</sup>

The alternative is to develop new models that deal directly with the wave equation producing a solution in the time domain without Fourier synthesis. A time-domain formulation of the PE was developed by McDonald and Kuperman,<sup>2</sup> and applied to both linear and nonlinear problems in ocean acoustics. This approach has been extended by Collins<sup>3</sup> to handle wide-angle problems with attenuation. The appeal of this approach is that it bypasses the extra steps of Fourier decomposing the source and synthesizing the field. At present, it is unclear if there is a gain or loss in speed by working directly in the time domain.

In this paper, we shall develop a formulation of the fast-field program that is marched directly in the time domain. The technique is analogous to that used by Alekseyev and Mikhaylenko<sup>4</sup> for Lamb's problem and extended to more general seismic problems by Olson *et al.*<sup>5</sup> The basic equations are developed in Sec. II, and a numerical discretization is described in Sec. III. Some extensions are developed in Sec. IV to handle a pulse-centered coordinate system, an angle-limited source, and attenuation. In Sec. V, examples of

the method are presented, including (1) a pulse propagating in free space, (2) a simple head-wave problem, and (3) a refracting problem with a hyperbolic cosine profile.

## I. GOVERNING EQUATIONS

The problem we consider is that of calculating the response to an isotropic point source in a stratified (i.e., range-independent) acoustic medium. The scenario is indicated schematically in Fig. 1. Within a layer the solution is governed by the acoustic wave equation

$$\nabla \cdot \left( \frac{1}{\rho} \nabla p \right) - \frac{1}{\rho c^2(z)} p_{tt} = - \frac{s(t)}{r} \delta(z - z_s, r), \quad (1)$$

where  $p(r, z, t)$  is the acoustic pressure as a function of depth  $z$ , range  $r$ , and time  $t$ . In addition,  $s(t)$  is the isotropic point source,  $\rho(z)$  is the density, and  $c(z)$  is the sound speed. To completely specify the problem, we require some boundary and initial conditions. We assume that the surface is a pressure-release boundary and that at some sufficiently great depth  $D$ , the boundary can be treated as perfectly rigid:

$$p(r, 0, t) = 0, \quad p_z(r, D, t) = 0. \quad (2)$$

Furthermore, we require

$$p(r, z, t), \quad \text{outgoing as } r \rightarrow \infty. \quad (3)$$

Finally, we assume that initially the medium is quiescent; i.e.,

$$p(r, z, 0) = p_t(r, z, 0) = 0. \quad (4)$$

When discontinuous interfaces are present, the wave equa-

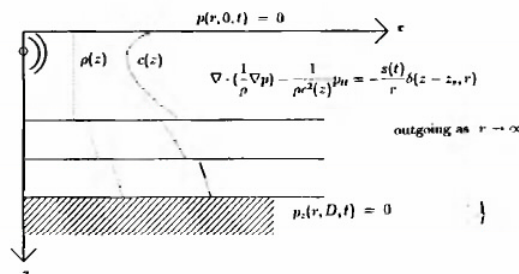


FIG. 1. Schematic of the range-independent environmental scenario.

tion applies within each smooth layer, and interface conditions requiring continuity of pressure and normal displacement are imposed.

The time-domain FFP is obtained by applying a Fourier–Bessel transform (in range) to Eq. (1). That is, we write

$$\hat{p}(k, z, t) = \int_0^\infty p(r, z, t) J_0(kr) r dr, \quad (5)$$

which leads to

$$\frac{\partial}{\partial z} \left( \frac{1}{\rho} \frac{\partial \hat{p}}{\partial z} \right) - \frac{k^2}{\rho} \hat{p} - \frac{1}{\rho c^2(z)} \hat{p}_n = -s(t) \delta(z - z_s), \quad (6)$$

together with the boundary and initial conditions

$$\hat{p}(r, 0, t) = \hat{p}_z(r, D, t) = 0, \quad \hat{p}(r, z, 0) = \hat{p}_t(r, z, 0) = 0. \quad (7)$$

Equations (6) and (7) are the governing equations for the time-marched FFP. If we were to go one step further and factor out an  $e^{i\omega t}$  time dependence, we would obtain the usual equations for the time-harmonic FFP.<sup>6</sup>

We observe that for any fixed  $k$ , Eq. (6) assumes the form of a vibrating string embedded in an elastic membrane.<sup>7</sup> (It is also a special case of a Klein–Gordon equation in quantum mechanics.) The parameter  $k$  then governs the restoring force of the surrounding elastic medium so that for  $k = 0$  we obtain the familiar equation for a vibrating string in free space.

These equations are solved for a sequence of  $k$  values, and then the pressure is evaluated using the inverse Fourier–Bessel transform:

$$p(r, z, t) = \int_0^\infty \hat{p}(k, z, t) J_0(kr) k dk. \quad (8)$$

For a line source one need only replace the Bessel transform by an ordinary Fourier transform.

## II. NUMERICAL ALGORITHM

Numerically, the problem is composed of two parts: the construction of the kernel  $\hat{p}(k, z, t)$  and the evaluation of the Fourier–Bessel transform. We shall describe each of these two steps in more detail.

### A. Evaluation of the kernel

In order to discretize Eq. (6), we employ finite elements in depth and finite differences in time. Thus we seek a solution

$$\hat{p}(z, t; k) = \sum_{i=1}^m p_i(t; k) \phi_i(z), \quad (9)$$

where  $\phi_i(z)$  is the familiar linear shape function (“hat” shaped):

$$\phi_i(z) = \begin{cases} \frac{z - z_{i-1}}{h_i}, & \text{for } z_{i-1} < z \leq z_i, \\ \frac{z_{i+1} - z}{h_{i+1}}, & \text{for } z_i < z \leq z_{i+1}, \\ 0, & \text{else,} \end{cases} \quad (10)$$

where  $h_i = z_i - z_{i-1}$  denotes the thickness of the  $i$ th element.

The details of what follows may be obtained from standard finite-element texts such as Refs. 8 and 9. One finds that the nodal pressures  $p_i(t)$  satisfy an equation of the form

$$\mathbf{K}\mathbf{p} - \mathbf{M}\mathbf{p}_n = \mathbf{s}(t), \quad (11)$$

where  $\mathbf{p}$  denotes the vector of nodal pressures. In addition,  $\mathbf{M}$  and  $\mathbf{K}$  are, respectively, the global mass and stiffness matrix obtained by summing the contributions of elemental mass and stiffness matrices, given by

$$\mathbf{K} = \sum_{e=1}^E L(\mathbf{K}_e), \quad \mathbf{M} = \sum_{e=1}^E L(\mathbf{M}_e). \quad (12)$$

Here,  $L(\cdot)$  is a locator function which maps a  $2 \times 2$  element matrix into the appropriate position in the global matrix. The elemental matrices are given by

$$\mathbf{K}_e = \frac{1}{h_e \rho^e} \begin{bmatrix} 1 & -1 \\ -1 & 1 \end{bmatrix} + \frac{h_e k^2}{6\rho^e} \begin{bmatrix} 3-\alpha & \alpha \\ \alpha & 3-\alpha \end{bmatrix}$$

and

$$\mathbf{M}_e = \frac{h_e}{6\rho^e c_e^2} \begin{bmatrix} 3-\alpha & \alpha \\ \alpha & 3-\alpha \end{bmatrix}.$$

If interfaces are present where the density or sound speed is discontinuous, the interface conditions of continuity of pressure and normal displacement are automatically imposed in this finite-element discretization.

For the time discretization, we employ the following finite-difference approximation:

$$\mathbf{K}[\beta \mathbf{p}^{j+1} + (1-2\beta)\mathbf{p}^j + \beta \mathbf{p}^{j-1}] - \mathbf{M} \frac{\mathbf{p}^{j+1} - 2\mathbf{p}^j + \mathbf{p}^{j-1}}{(\Delta t)^2} = \mathbf{s}^j, \quad (13)$$

where  $\mathbf{p}^j$  denotes the vector of nodal pressures at time step  $j$ . A Dirichlet boundary condition is easily imposed during the time marching by simply zeroing out the first or last component of the pressure vector. If no action is taken, then the Neumann boundary condition is the natural (automatically imposed) boundary condition.

The above discretization allows for two free parameters,  $\alpha$  and  $\beta$ , which control the “consistency” and the “explicitness.” Thus, choosing  $(\alpha, \beta) = (0, 0)$ , we obtain a lumped mass matrix and a fully explicit time integrator. This is convenient for parallel or pipelined computer architectures. In the Appendix we show that the explicit integrator is stable for

$$\Delta t < 1/\sqrt{c^2 [1/(\Delta z)^2 + k^2/4]}.$$

The  $(\alpha, \beta) = (1, 0.25)$  scheme is the consistent mass matrix combined with a trapezoidal time integrator. Every step requires the inversion of a tridiagonal matrix; however, (as shown in the Appendix), the method has the advantage of being unconditionally stable. We use this scheme for the advective problem which is described later.

### B. Evaluation of the spectral integral

As in the standard FFP, we shall take advantage of an FFT to evaluate the spectral integral at a number of points in

range. This technique was apparently first suggested by Marsh and Elam and developed for transmission loss modeling by DiNapoli. See Ref. 10 and references contained therein.

In order to obtain a suitable form, we replace the Bessel function by its asymptotic approximation and truncate the integral at some finite value. Thus we obtain

$$p(r,z,t) = \int_0^\infty \hat{p}(k,z,t) J_0(kr) k dk \quad (14)$$

$$\approx \sqrt{\frac{2}{\pi r}} \int_{K_{\min}}^{K_{\max}} \hat{p}(k,z,t) \cos(kr - \pi/4) \sqrt{k} dk. \quad (15)$$

The value of  $K_{\max}$  is chosen to sample the highest spatial frequency in the problem. Thus, if the source is bandlimited with upper frequency  $f_{\max}$ , then the shortest wavelength is  $c_{\min}/f_{\max}$ , where  $c_{\min}$  is the minimum sound speed present in the problem. So we set  $K_{\max} = 2\pi f_{\max}/c_{\min}$  to ensure that the pulse is adequately sampled in space. Finer sampling of the pressure field can be obtained by increasing  $K_{\max}$ ; however, for  $|k| > K_{\max}$  the kernel essentially vanishes and should simply be zeroed out. Conversely,  $K_{\min}$  is governed by the longest wavelength and for problems with a low-frequency cutoff can be set at  $K_{\min} = 2\pi f_{\min}/c_{\max}$ .

Unlike the time-harmonic FFP, this integral can normally be performed directly on the real axis. This is because the resulting pressure field is typically limited in space so that the kernel is bandlimited. Thus the kernel is evaluated for  $k_j = K_{\min} + j\Delta k$ , where  $\Delta k = 2\pi/R_{\max}$ , and  $R_{\max}$  is the maximum range to which the pulse will propagate before the calculation is terminated.

The FFT is efficient for problems where the field is desired at many ranges, e.g., for snapshots. When the field is needed at very few points (e.g., for calculating the received time series on a vertical array), we apply the trapezoidal method directly.

### III. EXTENSIONS

#### A. Pulse-centered coordinates

For certain kinds of problems, the computation time can be greatly reduced by setting up a coordinate system that moves with the pulse. This technique, applied successfully by McDonald and Kuperman<sup>2</sup> for the time-domain parabolic equation model, is especially useful when there is a spatially confined pulse moving with a roughly constant velocity. This is a case that is not uncommon for ocean acoustic problems.

There are two advantages which are derived from using a pulse-centered coordinate system. The first is that the number of  $k$ -space points is reduced because the pulse occupies a narrow range window. The second is that the accuracy of the time integration increases because in the moving frame the dependent variables evolve more gradually.

The first advantage seems at first trivial to realize. We assume that the pulse is confined to some range window  $[R_{\min}, R_{\max}]$ . From the usual sampling results, we find that the required  $k$ -space sampling is reduced to  $\Delta k = 2\pi/(R_{\max} - R_{\min})$ .

Unfortunately, there is a complication. Because of the

symmetry of the problem, what actually happens is that both a left- and right-traveling wave are generated. Assuming that we are interested in only the right-traveling pulse, then we must eliminate the left-traveling pulse to avoid folding (aliasing) it into the window of the right-traveling pulse. This can be done by modifying the source function so that it contains only positive frequencies (terms of the form  $e^{i\omega t}$ ) and then performing the spectral integral using only negative  $k$  values (terms of the form  $e^{-ikr}$ ). Thus the solution is represented as a sum of components of the form  $e^{i(\omega t - kr)}$ , which represent right-traveling waves.

A single sideband source function can be calculated by forming the so-called “pre-envelope” of the source, which is given by

$$s_+(t) = s(t) + i\hat{s}(t), \quad (16)$$

where  $\hat{s}(t)$  is the Hilbert transform of  $s(t)$ , which is given by

$$\hat{s}(t) = \frac{1}{\pi} \int_{-\infty}^{\infty} \frac{s(\tau)}{t - \tau} d\tau. \quad (17)$$

[The pre-envelope can also be calculated by forming the Fourier transform of  $s(t)$ , zeroing out the negative frequencies and transforming back to the time domain.] The resulting source function is complex so that it is then necessary to perform the time marching using complex arithmetic.

Finally, the spatial transform is performed using only negative  $k$  values as follows:

$$p(r,z,t) \approx \sqrt{\frac{1}{2\pi r}} \int_{K_{\min}}^{K_{\max}} \operatorname{Re}[\hat{p}(k,z,t)e^{-i(kr - \pi/4)}] \sqrt{k} dk. \quad (18)$$

In order to realize the second feature of actually doing the numerical integration in the moving frame, we introduce the pulse-centered coordinate system  $R = r - Vt$ , where  $V$  is the velocity of the moving reference frame. We take as a definition

$$p(R,z,t) = \sqrt{\frac{1}{2\pi r}} \int_{K_{\min}}^{K_{\max}} \hat{p}(k,z,t) e^{-i(kr - \pi/4)} \sqrt{k} dk, \quad (19)$$

where  $\hat{p}(k,z,t)$  satisfies Eq. (6). We now seek the equation for an analogous function  $\hat{q}(k,z,t)$ , which transformed yields the pressure in the moving reference frame  $p(R,z,t)$ . By definition,

$$\begin{aligned} p(R,z,t) &= \sqrt{\frac{1}{2\pi r}} \int_{K_{\min}}^{K_{\max}} \hat{p}(k,z,t) e^{-i[k(R + Vt) - \pi/4]} \sqrt{k} dk \\ &= \sqrt{\frac{1}{2\pi r}} \int_{K_{\min}}^{K_{\max}} \hat{q}(k,z,t) e^{-i(kR - \pi/4)} \sqrt{k} dk, \end{aligned} \quad (20)$$

where  $\hat{q} = \hat{p}e^{-ikVt}$ . Making this change of variables in Eq. (6), we find that  $\hat{q}$  must satisfy a convected form of the time-marched FFP:

$$\begin{aligned} \frac{\partial}{\partial z} \left( \frac{1}{\rho} \frac{\partial}{\partial z} \hat{q} \right) - \frac{k^2}{\rho} \left( 1 - \frac{V^2}{c^2} \right) \hat{q} - \frac{2ikV}{\rho c^2} \hat{q}_t - \frac{1}{\rho c^2} \hat{q}_{tt} \\ = -s(t)e^{-ikVt} \delta(z - z_s). \end{aligned} \quad (21)$$

This equation can also be obtained by introducing the change of variables  $R = r - Vt$  into the original wave equation to produce the following convected wave equation:

$$\nabla \cdot [ (1/\rho) \nabla q ] - \{ 1/[\rho c^2(z)] \} (q_u - 2Vq_{Rt} + V^2 q_{RR}) = - [s(t)/(R + Vt)] \delta(z - z_s, R + Vt). \quad (22)$$

For a line source the Fourier transform then yields Eq. (21). For a point source some care is required to take account of the approximate Fourier-Bessel transform.

### B. Angular filtering

An angle-limited source can be useful either for eliminating bottom reflections or for reducing the CPU time in problems where higher-angle energy is unimportant. In the frequency-domain FFP this is accomplished by setting  $K_{\min} = \omega/c_{\max}$ , where  $c_{\max}$  is the highest phase velocity to be included. Thus the limits of integration are varied as a function of frequency. (The corresponding source angle can be computed from Snell's law.) In the time-marched FFP an angle-limited source can be produced by low-pass filtering the source function. The cutoff frequency is varied as a function of  $k$  according to  $\omega_{\max} = kc_{\max}$ .

In experimental problems, the received time series is often filtered by the measurement apparatus. In such cases, it is convenient to apply the corresponding filter directly to the source time series. This reduces the spatial and temporal sampling requirements for the numerical integration.

### C. Attenuation

There is a great deal of uncertainty as to the "correct" manner for treating dissipative effects in ocean sediments. A fairly general form of a damped-wave equation is given by

$$\left( 1 + d(z,t) * \frac{\partial}{\partial t} \right) \nabla \cdot \left( \frac{1}{\rho} \nabla p \right) - \frac{1}{\rho c^2(z)} p_u = - [s(t)/r] \delta(z - z_s, r), \quad (23)$$

where  $*$  denotes the convolution operator. From a numerical point of view, the inclusion of this convolution operator means that, in general, a single step forward in time requires the entire time history of the field. Specifying the kernel of the convolution,  $d(z,t)$  is equivalent to specifying the frequency dependence of the damping.

A useful simplification is obtained by assuming the kernel takes the form of a delta function in time. In other words, we write  $d(z,t) = d(z)\delta(t)$ , obtaining

$$\left( 1 + d(z) \frac{\partial}{\partial t} \right) \nabla \cdot \left( \frac{1}{\rho} \nabla p \right) - \frac{1}{\rho c^2(z)} p_u = - [s(t)/r] \delta(z - z_s, r), \quad (24)$$

which is the Voigt model for damping. As before, we apply a Fourier transform to obtain the FFP form:

$$\mathcal{L}\hat{p} + d(z) \mathcal{L}\hat{p}_t - \{ 1/[\rho c^2(z)] \} \hat{p}_u = - s(t) \delta(z - z_s), \quad (25)$$

where  $\mathcal{L}$  is the operator

$$\mathcal{L}\hat{p} = \frac{\partial}{\partial z} \left( \frac{1}{\rho} \frac{\partial}{\partial z} \hat{p} \right) - \frac{k^2}{\rho} \hat{p}. \quad (26)$$

The convected form is obtained by making the substitution  $\hat{q} = \hat{p} e^{-ikVt}$ :

$$\left( [1 + ikVd] \mathcal{L} + \frac{k^2 V^2}{\rho c^2} \right) \hat{q} + \left( d(z) \mathcal{L} - \frac{2ikV}{\rho c^2} \right) \hat{q}_t - \{ 1/[\rho c^2] \} \hat{q}_u = - s(t) e^{-ikVt} \delta(z - z_s). \quad (27)$$

We use a simple centered-difference approximation for the time derivative in the damping term so that the resulting marching equation remains a three-step recursion.

Note that by factoring out a time dependence of the form  $e^{i\omega t}$ , Eq. (23) assumes the form

$$[1 + i\omega d(z)] \nabla \cdot [ (1/\rho) \nabla p ] - \{ \omega^2 / [\rho c^2(z)] \} p = [s(\omega)/r] \delta(z - z_s, r). \quad (28)$$

This is a (variable density) Helmholtz equation with a complex sound speed  $\hat{c}$  given by

$$\hat{c}^2(z, \omega) = [1 + i\omega d(z)] c^2(z). \quad (29)$$

Thus, for low frequencies, the imaginary part of the sound speed grows linearly in frequency, and the attenuation coefficient grows in proportion to the frequency squared. Experimental data in the 10- to 1000-Hz region seem to suggest a frequency dependence somewhere between linear and quadratic.<sup>11</sup>

## IV. EXAMPLES

### A. A pulse in free space

As a first example, we consider the propagation of a pseudo-Gaussian pulse in free space. The particular waveform used is given by

$$s(t) = \begin{cases} 0.75 - \cos 2\pi f_c t + 0.25 \cos 4\pi f_c t, & \text{for } 0 < t < 1/f_c, \\ 0, & \text{else,} \end{cases} \quad (30)$$

where  $f_c$  is a frequency that characterizes the pulse length. We use  $f_c = 100$  Hz. (The model is of course capable of handling an arbitrary pulse time series. A number of such "canned" source functions given in Ref. 12 have been implemented.)

As illustrated schematically in Fig. 2 we consider the field received on an array located 100 m from the source. The exact solution to this problem is given by

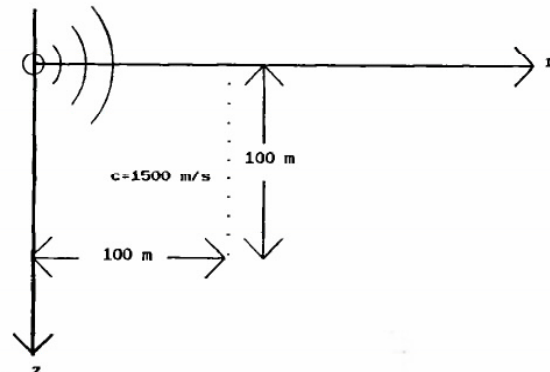


FIG. 2. The free-space problem.

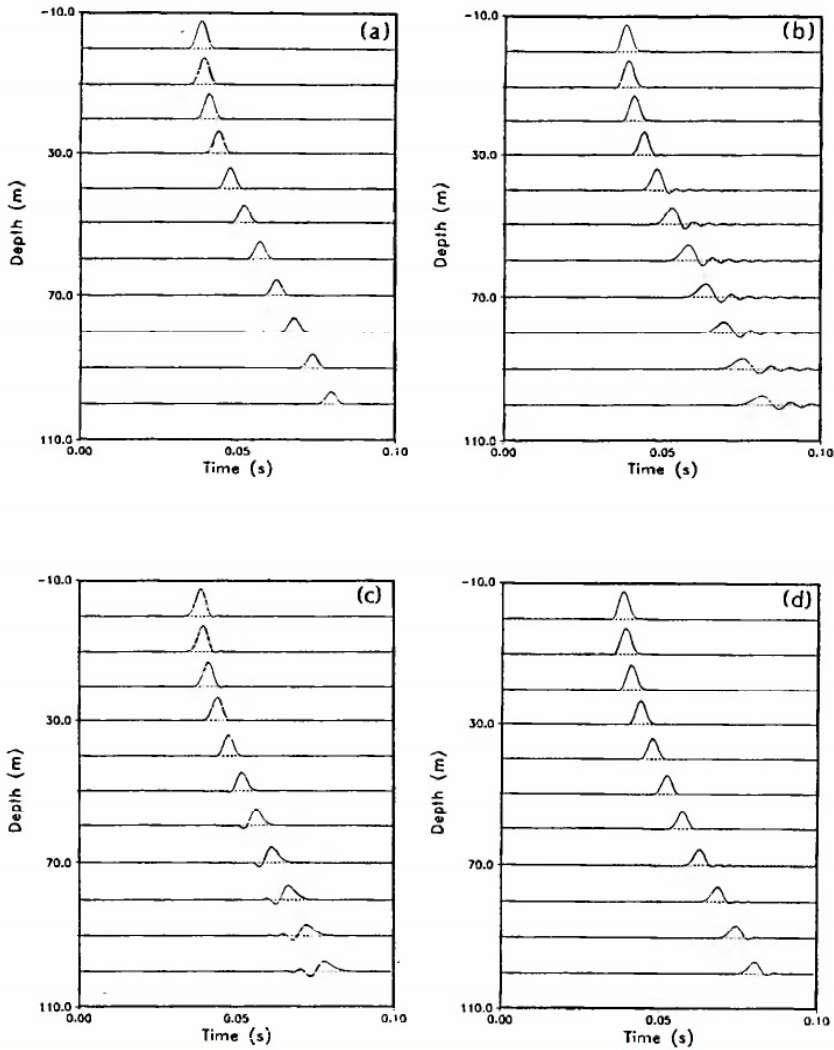


FIG. 3. Received time series for the free-space problem calculated using (a) the analytic solution, (b) the explicit scheme with  $\Delta z = 2$  m, (c) the implicit scheme with  $\Delta z = 2$  m, and (d) the explicit scheme with a reduced  $\Delta z = 1$  m

$$p(r, z, t) = \frac{s(t - r_s/c_0)}{4\pi r_s}, \quad (31)$$

where  $r_s = \sqrt{r^2 + z^2}$  is the slant range to the receiver, and  $c_0$  is the sound speed, which we set at 1500 m/s. Thus the time series at each receiver is a replica of the source function, but delayed according to the travel time to that particular receiver and scaled according to a spherical spreading law. This solution is plotted in Fig. 3(a).

In Fig. 3(b) we plot the results obtained using the time-marched FFP with a grid spacing of 2 m and using the explicit (0,0) scheme (lumped mass/explicit time integration). Dirichlet conditions have been applied at a sufficient distance from the source (200 m) to avoid the pulse interact-

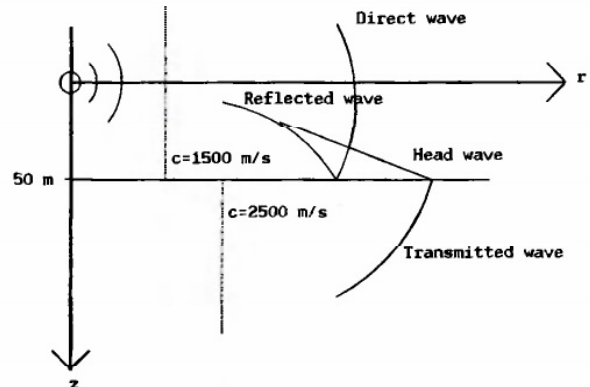


FIG. 4. Environmental scenario for the head-wave problem.

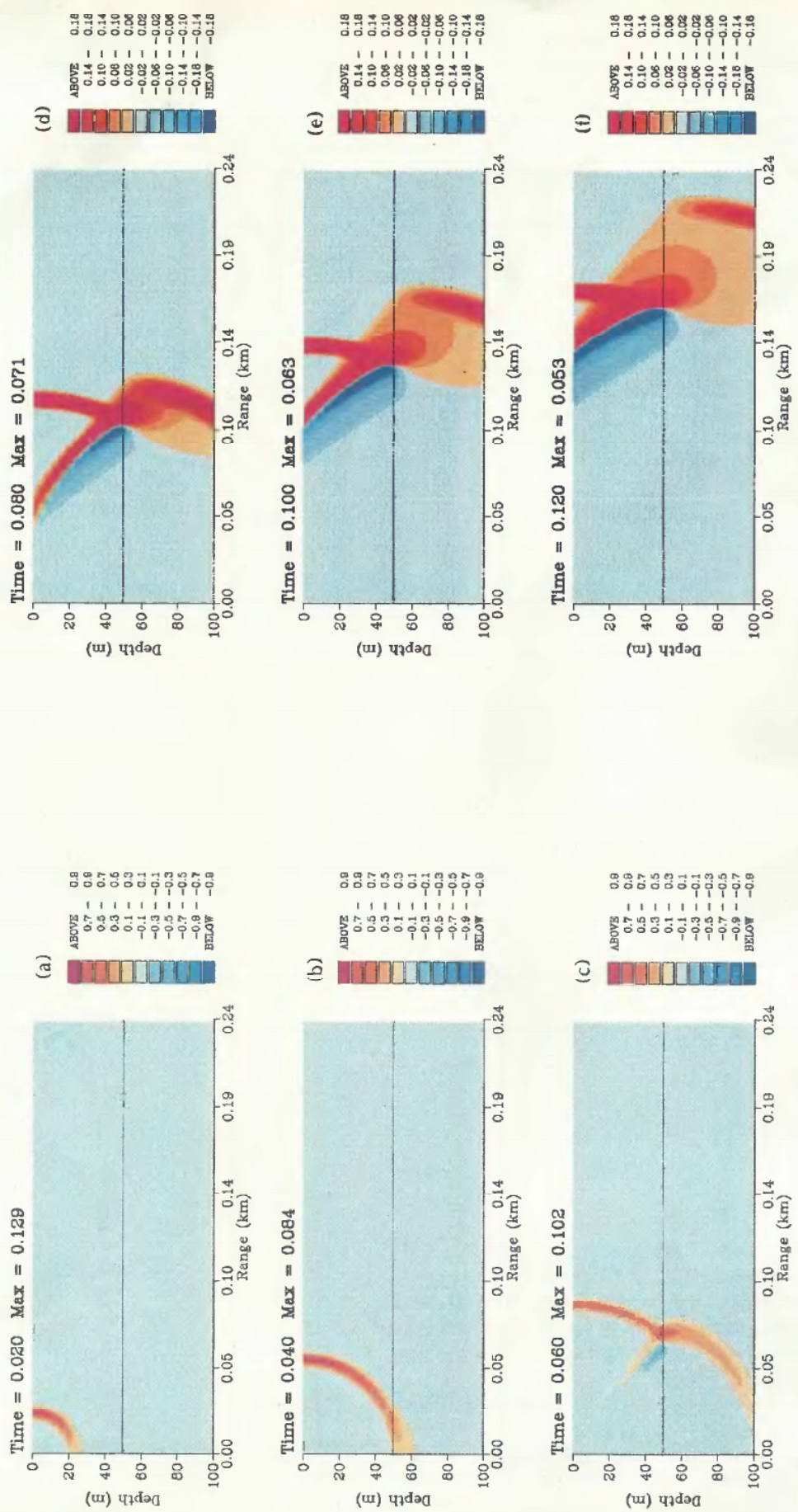


FIG. 5. Snapshots of the pulse for the head-wave problem.

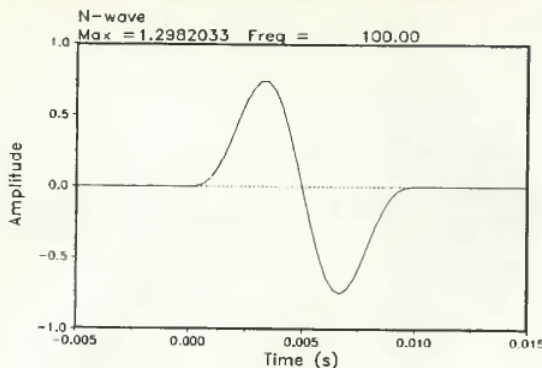


FIG. 6. Plot of the derivative of the pseudo-Gaussian wave.

ing with the boundary. The time step is set at 0.95 times the maximum stable time step, and the same step is used for each spectral component. With this grid spacing we have a little over seven points per wavelength at the 100-Hz characteristic frequency of the pulse. The numerical results show a well-known characteristic of such finite-element or finite-difference schemes: that of numerical dispersion. This aspect is discussed in more detail by Belytschko and Mullen<sup>13</sup> and by Trefethen.<sup>14</sup>

The dispersion characteristics are, of course, dependent on the particular difference scheme which is used. Switching to the implicit (1,0.25) scheme (consistent mass/trapezoidal integration), we obtain the results in Fig. 3(c) where now the ripple precedes the true solution. In both cases, however, we can obtain a suitably accurate solution simply by refining the mesh. In Fig. 3(d) we use the explicit scheme with a mesh width refined to 1 m (15 points per wavelength), which yields a solution that is difficult to distinguish from the exact solution.

At this time, we are open-minded about how to choose these various parameters. The implicit schemes seem to have won little favor for higher-dimensional problems due to the costs of solving the linear system at each step; however, this

is not an important consideration for our problem where we obtain tridiagonal matrices. Nevertheless, the explicit scheme would seem to be attractive for parallel or pipeline architectures. In terms of minimizing the dispersion characteristics, one has several parameters to consider. This includes  $(\alpha, \beta)$  for the basic discretization as well as the time step, which can easily be adjusted differently for each spectral component. There is also the possibility of adjusting the finite-element grid as well as the convection velocity  $V$ . In some problems it may be useful to adjust several of these parameters dynamically or as a function of the spectral component  $k$ .

### B. A head-wave problem

We next modify the previous problem by introducing a faster half-space with a velocity of 2500 m/s located 50 m below the source as indicated in Fig. 4. The time evolution of the field is plotted in Fig. 5 for a sequence of times from 20 to 120 ms. Note that the pressure has been normalized so that the maximum is unity and also multiplied by a factor of  $\sqrt{r}$  to compensate for cylindrical spreading.

In the initial frame we see a spherical wave since the pulse has not yet contacted the interface. In Fig. 5(b) the pulse is just beginning to interact with the lower half-space, and by Fig. 5(c) the effects on the transmitted wave are clearly visible. Since the sound speed is higher in the lower half-space, the pulse is longer in the bottom than in the top. The transmission coefficient is less than unity so that the transmitted wave shows a decreased amplitude relative to the direct wave.

The reflected wave shows a more complicated structure with a region of negative pressure trailing the leading edge. The phase of the reflection coefficient for a half-space is neither  $0^\circ$  nor  $180^\circ$ . A  $90^\circ$  phase change would yield a Hilbert transform of the pulse with the inverted trailer. However, the half-space is even more complicated in that the phase is angle dependent. Finally, we note that the critical angle effect shows up in the reflected wave: At steep angles there is virtually no reflected energy.

In Fig. 5(d)–(f) we can see the wave in the lower half-

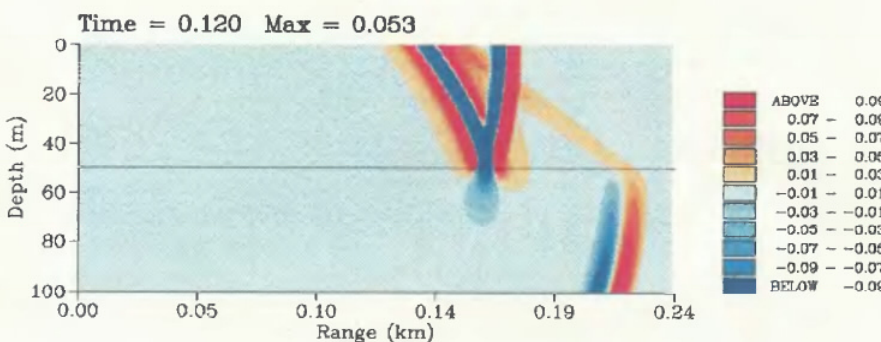


FIG. 7. Field after 0.120 s using the-source wavelet of Fig. 6.

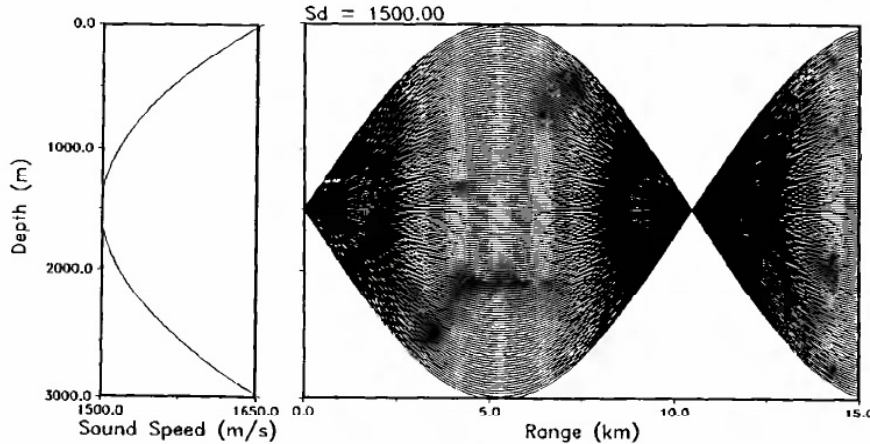


FIG. 8. Ray trace for the hyperbolic cosine profile.

space pulling ahead of the direct wave due to the greater wave speed in the bottom. (Note that we have changed the color scale in order to highlight the weak head-wave arrival.) The direct wave in the upper half-space carries with it a “direct-wave root”<sup>15</sup> which protrudes into the lower half-space.

The wave front of the head wave is also clearly visible forming a line segment starting from the transmitted wave in the lower half-space touching tangentially the reflected wave front. (This is indicated schematically in Fig. 4.) The head wave has a well-defined leading edge behind which is a region of higher pressure with no clearly defined termination. We remind that the time series for the head wave is roughly a convolution of the source time series  $s(t)$  with the Heaviside function  $H(t)$ . Thus, behind the wave front, the received time series approaches the integral of the source function. (We refer the reader to the text of Aki and Richards<sup>16</sup> for a readable mathematical analysis of the head wave.) Any source with a component at zero frequency will leave a non-decaying tail in its wake.

Conversely, by using a source with no DC level, we can obtain a head wave without a tail. As an example, we consider the wavelet given by

$$s(t) = \begin{cases} \sin 2\pi f_c t - 0.5 \sin 4\pi f_c t, & \text{for } 0 < t < 1/f_c, \\ 0, & \text{else,} \end{cases} \quad (32)$$

and plotted in Fig. 6. (This wave is proportional to the derivative of the pseudo-Gaussian pulse previously considered.) After 0.12 s we obtain the snapshot shown in Fig. 7. The reflected and transmitted waves show the positive leader and negative trailer of the original wavelet. The head wave is an integrated version of the source wavelet and therefore has roughly the form of a pseudo-Gaussian pulse. Note that the amplitude of the head wave increases as we move away from the interface toward the point of contact with the reflected wave.

### C. The hyperbolic cosine profile

As a final example, we consider a hyperbolic cosine profile given by

$$c(z) = 1500 \cosh [0.0003(z - 1500)]. \quad (33)$$

This problem has been previously treated by Tolstoy *et al.*<sup>17</sup> for time-harmonic forcing. The attraction for our purposes is that the effects of the refraction are particularly simple. The ray trace shown in Fig. 8 illustrates that the rays refocus perfectly at distances of about every 10 km.

The source time series is the same “pseudo-Gaussian” used for the previous problem, but with the central frequency decreased to 5 Hz. Unlike the previous problem we allow the pulse to reflect off the ocean surface and ocean bottom located at  $z = 0$  and 3000 m, respectively. These boundaries have both been treated as pressure-release surfaces.

The sequence of snapshots in Fig. 9 shows the development of the field over a period of about 10 s. After 3 s the initially spherical wave has flattened out due to the refractive effects as shown in Fig. 9(a). Behind the direct wave we see the surface and bottom reflections coming in with an inverted phase. In the next frame the curvature of the wave front becomes inverted as the wave begins to converge toward the focal point. In Fig. 9(c) the wave front has reached the approximate location of the focal point, and the peak amplitude is consequently much higher. Finally, in Fig. 9(d), the wave front has passed through the focal point and begins to diverge again. The wave front has been distorted as a result of its passage through the focus and shows an in-phase leading wave and an out-of-phase trailer. Roughly, the wave is phase shifted by 90° every time it passes through the foci so that after two cycles a phase-inverted version of the pulse is recovered.

### V. SUMMARY AND CONCLUSIONS

We have described a fast-field program that is marched directly in the time domain and suitable for typical problems in underwater acoustics. The algorithm allows for multiple layers within which the sound speed is an arbitrary smooth function of depth. At the interfaces between layers we allow for possible discontinuities in material properties. Additional terms have also been included to account for attenu-

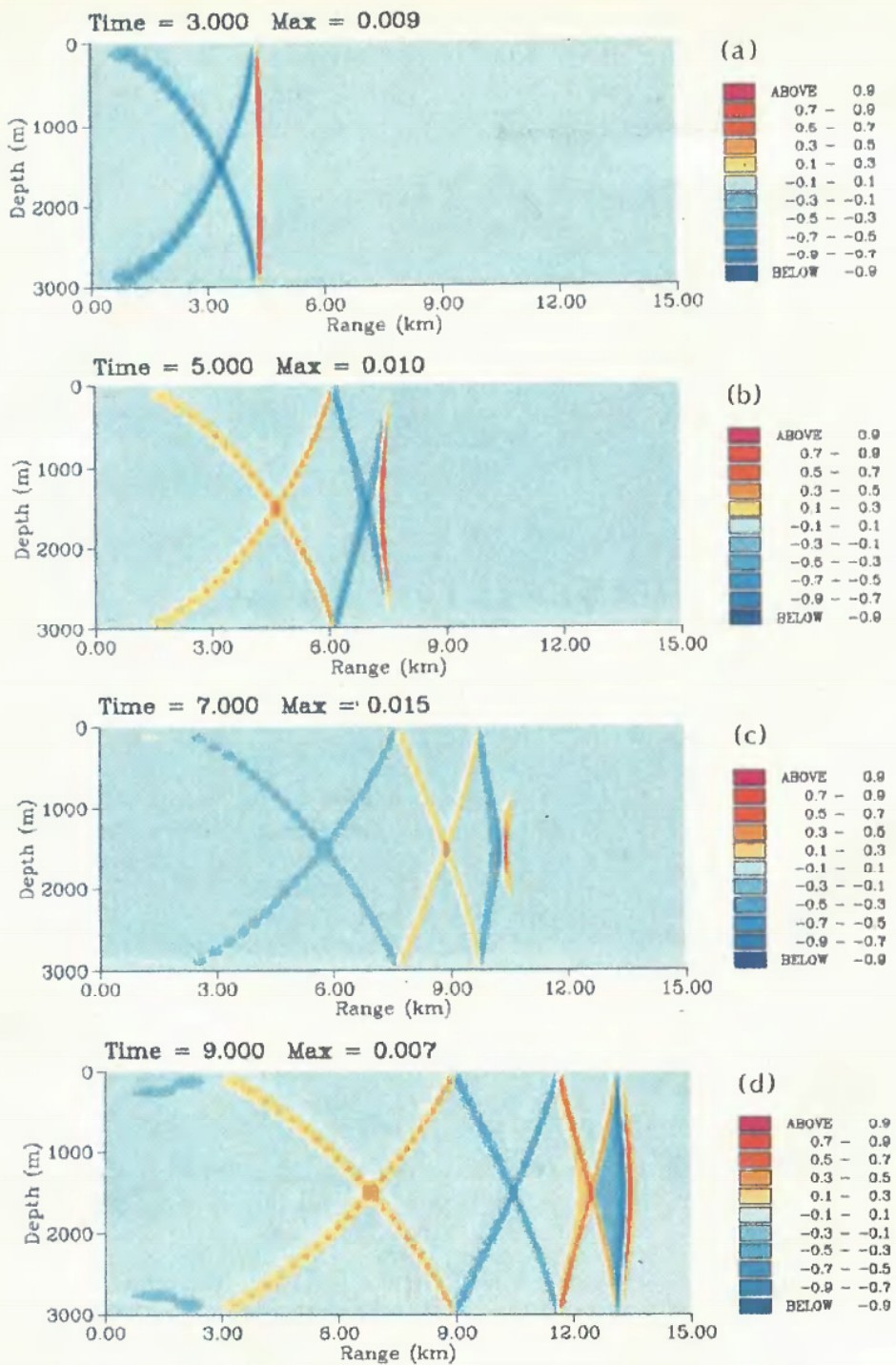


FIG. 9. Snapshots of the pulse propagating in the hyperbolic cosine profile.

ation and for advection which is useful for providing a coordinate system which frames the pulse.

There remain a number of questions for further research. First, it would be desirable to implement the more flexible loss term with arbitrary frequency dependence. Second, there are several possible avenues for increasing the efficiency of the algorithm. For instance, the time step and depth step could be varied as a function of time and spectral component. Higher-order discretizations could be extreme-

ly useful. Finally, it would be desirable to treat mixed acoustic and elastic problems.

#### APPENDIX A: STABILITY FOR THE EXPLICIT SCHEME

For the explicit scheme, the equation

$$\frac{\partial}{\partial z} \left( \frac{1}{\rho} \frac{\partial}{\partial z} \hat{p} \right) - \frac{k^2}{\rho} \hat{p} - \frac{1}{\rho c^2(z)} \hat{p}_u = 0 \quad (\text{A1})$$

is discretized by

$$\mathbf{K}\mathbf{p}^j - \mathbf{M}[(\mathbf{p}^{j+1} - 2\mathbf{p}^j + \mathbf{p}^{j-1})/(\Delta t)^2] = 0, \quad (\text{A2})$$

where  $\mathbf{K}$  is a tridiagonal matrix, and  $\mathbf{M}$  is a diagonal matrix. The  $i$ th rows of  $\mathbf{K}$  and  $\mathbf{M}$  are given by

$$\begin{aligned} k_{i,i-1} &= 1/(\rho_{i-1}h_{i-1}), \\ k_{i,i} &= \left( \frac{-1}{\rho_{i-1}h_{i-1}} - \frac{k^2h_{i-1}}{\rho_{i-1}} \right) + \left( \frac{-1}{\rho_i h_i} - \frac{k^2h_i}{\rho_i} \right), \\ k_{i,i+1} &= 1/(\rho_i h_i), \\ m_{i,i} &= \frac{1}{2} \left( \frac{h_{i-1}}{\rho_{i-1}c_{i-1}^2} + \frac{h_i}{\rho_i c_i^2} \right), \end{aligned} \quad (\text{A3})$$

where  $h_i$ ,  $c_i$ , and  $\rho_i$  denote the thickness, sound speed, and density of the  $i$ th element, respectively. For simplicity, we shall ignore the boundary conditions which modify the first and last rows of these matrices.

The general solution of this recursion can be represented as a sum of terms  $\xi^j \mathbf{p}$  where  $\xi$  and  $\mathbf{p}$  satisfy the algebraic eigenvalue problem:

$$\{\mathbf{M}\xi^2 - [2\mathbf{M} + \mathbf{K}(\Delta t)^2]\xi + \mathbf{M}\}\mathbf{p} = 0. \quad (\text{A4})$$

For stability we require that an initial disturbance should remain unamplified, i.e.,  $|\xi| \leq 1$ .

Let  $\lambda = i(\xi + 1)/(\xi - 1)$ , which implies  $\xi = (\lambda + i)/(\lambda - i)$ . Since the bilinear transformation maps the unit circle into the lower half-plane, we will want to show that all  $\lambda$  lie in the lower half plane. Substituting, we obtain

$$[4\mathbf{M}/(\Delta t)^2 + \mathbf{K}]\mathbf{p} = -\lambda^2 \mathbf{K}\mathbf{p}. \quad (\text{A5})$$

Now, this is a generalized algebraic eigenvalue problem of the form  $\mathbf{Ax} = \kappa \mathbf{Bx}$  with  $\mathbf{A}$  symmetric and  $\mathbf{B}$  symmetric and positive definite. Thus all the eigenvalues are real. In addition, by the inertia theorem the eigenvalues of this generalized problem have the same signs as the eigenvalues of  $\mathbf{A}$  itself. So it will be sufficient to establish a condition which ensures that all eigenvalues of  $\mathbf{A}$  are positive. By Gershgorin's theorem, the eigenvalues lie within the union of discs:

$$|4m_{i,i}/(\Delta t)^2 + k_{i,i} - \lambda^2| < k_{i,i-1} + k_{i,i+1}. \quad (\text{A6})$$

Thus we require that all discs lie to the right of the origin:

$$4m_{i,i}/(\Delta t)^2 + k_{i,i} - (k_{i,i-1} + k_{i,i+1}) > 0. \quad (\text{A7})$$

Solving for  $\Delta t$ , we obtain the stability condition

$$(\Delta t)^2 < \min_i \frac{4m_{i,i}}{-k_{i,i} + (k_{i,i-1} + k_{i,i+1})} \quad (\text{A8})$$

or

$$(\Delta t)^2 < \min_i \left[ \left( \frac{2h_{i-1}}{\rho_{i-1}c_{i-1}^2} + \frac{2h_i}{\rho_i c_i^2} \right) / \left( \frac{2}{\rho_{i-1}h_{i-1}} + \frac{k^2h_{i-1}}{\rho_{i-1}} + \frac{2}{\rho_i h_i} + \frac{k^2h_i}{\rho_i} \right) \right]. \quad (\text{A9})$$

If the mesh is equispaced, and the density and sound speed constant, this reduces to

$$(\Delta t)^2 < 1/c^2 \left( \frac{1}{h^2} + \frac{k^2}{4} \right). \quad (\text{A10})$$

Note that for  $k = 0$  we recover the usual Courant–Friedrichs–Lowy condition for a vibrating string.

## APPENDIX B: STABILITY FOR THE IMPLICIT SCHEME

For the implicit scheme, the equation

$$\begin{aligned} \frac{\partial}{\partial z} \left( \frac{1}{\rho} \frac{\partial}{\partial z} \hat{p} \right) - \frac{k^2}{\rho} \left( 1 - \frac{V^2}{c^2} \right) \hat{p} - \frac{2ikV}{\rho c^2} \hat{p}_t \\ - \frac{1}{\rho c^2(z)} \hat{p}_{tt} = 0 \end{aligned} \quad (\text{B1})$$

is discretized using

$$\begin{aligned} \mathbf{K} \frac{\mathbf{p}^{j+1} + 2\mathbf{p}^j + \mathbf{p}^{j-1}}{4} + ikVM \frac{\mathbf{p}^{j+1} - \mathbf{p}^{j-1}}{2\Delta t} \\ - \mathbf{M} \frac{\mathbf{p}^{j+1} - 2\mathbf{p}^j + \mathbf{p}^{j-1}}{(\Delta t)^2} = 0. \end{aligned} \quad (\text{B2})$$

For an isovelocity, isodensity problem with an equispaced grid, the matrices  $\mathbf{K}$  and  $\mathbf{M}$  have elements

$$\begin{aligned} k_{i,i-1} &= \frac{1}{\rho h} - \left( \frac{\alpha}{6} \right) \frac{k^2(1 - V^2/c^2)h}{\rho}, \\ k_{i,i} &= \frac{-2}{\rho h} - \left( \frac{6-2\alpha}{6} \right) \frac{k^2(1 - V^2/c^2)h}{\rho}, \\ k_{i,i+1} &= \frac{1}{\rho h} - \left( \frac{\alpha}{6} \right) \frac{k^2(1 - V^2/c^2)h}{\rho}, \\ m_{i,i-1} &= (\alpha/6)[h/(\rho c^2)], \\ m_{i,i} &= [(6-2\alpha)/6][h/(\rho c^2)], \\ m_{i,i+1} &= (\alpha/6)[h/(\rho c^2)]. \end{aligned} \quad (\text{B3})$$

In the following proof we shall require only that  $-\mathbf{K}$  and  $\mathbf{M}$  are symmetric and positive definite. This poses the restriction that the convection velocity  $V$  should be less than the slowest element sound speed, but allows for depth-dependent material properties and meshes.

The corresponding eigenvalue problem is

$$[\mathbf{K}(\xi + 1)^2/4 + ikVM(\xi^2 - 1)/\Delta t \\ - \mathbf{M}(\xi - 1)^2/(\Delta t)^2]\mathbf{p} = 0. \quad (\text{B4})$$

As before, we make the bilinear substitution  $\lambda = i[(\xi + 1)/(\xi - 1)]$  to obtain,

$$[-\mathbf{K}\lambda^2 - (4kVM/\Delta t)\lambda - 4\mathbf{M}/(\Delta t)^2]\mathbf{p} = 0. \quad (\text{B5})$$

Introducing the vector,  $\mathbf{q} = \mathbf{W}'\mathbf{p}$ , where  $\mathbf{W}$  is defined by  $-\mathbf{K} = \mathbf{WW}'$ , this can be rewritten as

$$[\lambda^2 - (4kVB/\Delta t)\lambda - 4\mathbf{B}/(\Delta t)^2]\mathbf{q} = 0, \quad (\text{B6})$$

where  $\mathbf{B} = \mathbf{W}^{-1}\mathbf{M}\mathbf{W}^{-1}$  is a symmetric positive definite matrix. (This follows since  $\mathbf{M}$  is symmetric positive definite and  $\mathbf{B}$  is related to  $\mathbf{M}$  by a congruence transformation.) We denote the eigenvalues and eigenvectors of  $\mathbf{B}$  by  $\beta_i$  and  $\mathbf{q}_i$ , respectively. Evidently,  $\mathbf{q}_i$  is also an eigenvector of Eq. (6) with the corresponding eigenvalues satisfying

$$\lambda^2 - (4kV\beta_i/\Delta t)\lambda - 4\beta_i/(\Delta t)^2 = 0. \quad (\text{B7})$$

The discriminant of this equation is positive and so all  $\lambda_i$  are real. Thus the difference equations are *unconditionally stable*.

<sup>1</sup>F. B. Jensen (personal communication) (1989).

<sup>2</sup>B. E. McDonald and W. A. Kuperman, "Time domain formulation for pulse propagation including nonlinear behavior at a caustic," *J. Acoust.*

- Soc. Am. **81**, 1406–1417 (1987).
- <sup>3</sup>M. D. Collins, “The time-domain solution of the wide-angle parabolic equation including the effects of sediment dispersion,” J. Acoust. Soc. Am. **84**, 2114–2125 (1988).
- <sup>4</sup>A. S. Alekseyev and B. G. Mikhaylenko, “Solution of Lamb’s problem for a vertically inhomogeneous elastic halfspace,” Izv. Earth Phys. **12**, 11–25 (1976).
- <sup>5</sup>A. H. Olson, J. A. Orcutt, and G. A. Frazier, “The discrete wavenumber/finite element method for synthetic seismograms,” Geophys. J.R. Astron. Soc. **77**, 421–460 (1984).
- <sup>6</sup>H. Schmidt and F. B. Jensen, “A full wave solution for propagation in multilayered viscoelastic media with application to Gaussian beam reflection at fluid/solid interfaces,” J. Acoust. Soc. Am. **83**, 571–587 (1985).
- <sup>7</sup>P. M. Morse and H. Feshback, *Methods of Theoretical Physics* (McGraw-Hill, New York, 1953), pp. 138–141.
- <sup>8</sup>O. C. Zienkiewicz, *The Finite Element Method* (McGraw-Hill, London, 1977).
- <sup>9</sup>E. B. Becker, G. F. Carey, and J. T. Oden, *Finite Elements: An Introduction* (Prentice-Hall, Englewood Cliffs, NJ, 1981).
- <sup>10</sup>F. R. DiNapoli and R. L. Deavenport, “Theoretical and numerical Green’s function field solution in a plane multilayered medium,” J. Acoust. Soc. Am. **67**, 92–105 (1980).
- <sup>11</sup>J. Zhou, X. Zhang, P. H. Rogers, and J. Jarzynski, “Geoacoustic parameters in a stratified sea bottom from shallow-water acoustic propagation,” J. Acoust. Soc. Am. **82**, 2068–2074 (1987).
- <sup>12</sup>H. Schmidt, “SAFARI (Seismo-acoustic fast field algorithm for range-independent environments) user’s guide,” SACLANT Undersea Res. Centre Rep. SR-113 (1988).
- <sup>13</sup>T. Belytschko and R. Mullen, “On dispersive properties of finite element solutions,” in *Modern Problems in Elastic Wave Propagation*, edited by J. Miklowitz and J. Achenbach (Wiley, New York, 1978), pp. 67–82.
- <sup>14</sup>L. N. Trefethen, “Group velocity in finite difference schemes,” SIAM Rev. **24**, 113–136 (1982).
- <sup>15</sup>R. A. Stephen and S. T. Bolmer, “The direct wave root in marine seismology,” Bull. Seismol. Soc. Am. **75**, 57–67 (1985).
- <sup>16</sup>K. Aki and P. G. Richards, *Quantitative Seismology* (Freeman, New York, 1980), pp. 211–214.
- <sup>17</sup>A. Tolstoy, D. H. Berman, and E. R. Franchi, “Ray theory versus the parabolic equation in a long-range ducted environment,” J. Acoust. Soc. Am. **78**, 176–189 (1985).